Journal of Materials Chemistry A

ROYAL SOCIETY OF CHEMISTRY

PAPER

View Article Online
View Journal | View Issue

Open Access Article. Published on 31 October 2025. Downloaded on 6/15/2026 3:06:40 AM. This article is licensed under a Creative Commons Attribution-NonCommercial 3.0 Unported Licence.

Check for updates

Cite this: *J. Mater. Chem. A*, 2025, **13**, 42028

Improved stability and selectivity of $CuFe_2O_4$-based catalysts for photoelectrochemical CO_2-to-acetate conversion

Naohiko Kato, * Shu Saeki, Yusaku F. Nishimura, Yasuhiko Takeda and Shinya Moribe

Received 29th July 2025
Accepted 29th October 2025

DOI: 10.1039/d5ta06122a

rsc.li/materials-a

It is well known that photocathodes using $CuFeO_2$-based catalysts produce acetate *via* photoelectrochemical (PEC) CO_2 reduction. However, these catalysts suffer from low stability; the PEC activities rapidly decrease during the operation. To solve this problem, we developed a $CuFe_2O_4$-based catalyst. The photocathodes using the new catalyst achieved significantly higher stability for acetate production along with higher faradaic efficiencies (FE) exceeding 90%, compared with the conventional $CuFeO_2$-based photocathodes. *Operando* XAFS analyses and complementary techniques revealed that a considerable fraction of the Cu species were reduced to metal Cu in $CuFeO_2$, while the Fe species were leached into the electrolyte during the PEC operation, which is the cause of the low stability. By contrast, $CuFe_2O_4$ was stable; no change in the oxidation state of Cu or no leaching of Fe was observed. A mixture of $CuFe_2O_4$ and CuO increased the current density compared with that of the single-phase $CuFe_2O_4$ catalyst. Spectroscopic analyses of electronic states determined the energy levels of $CuFe_2O_4$ and CuO, indicating that $CuFe_2O_4$ could possess higher FEs than $CuFeO_2$, and that electrons photoexcited in CuO also could be consumed for acetate production after migrating to $CuFe_2O_4$. Thus, CuO functioned as a conductive additive and increased the photocurrents while retaining high FEs. However, the long-term stability of CuO was not sufficiently high. Hence, replacements of CuO with a more stable conductive additive are needed for fully exploiting the high stability and selectivity of $CuFe_2O_4$.

1. Introduction

Artificial photosynthesis is a promising means for converting CO_2 and water into useful organic compounds using solar energy, and, hence, has been the subject of vigorous research.[1–11] It has been developed in recent years from two perspectives: fixation of CO_2 and substantial reduction in emissions, and storage of solar energy. Large-scale devices have also been demonstrated toward practical application,[12–14] along with material developments for higher activity and stability using small-sized devices.[15,16] Artificial-photosynthetic reactions that selectively produce C1 compounds including formate and carbon monoxide have been established. Indeed, a 1 m^2 system that combines an electrochemical (EC) reactor using a metal-complex polymer catalyst and silicon solar cells achieved a high solar-to-formate energy conversion efficiency of 10.5%.[14]

On the other hand, Cu-based catalysts produce higher value-added C2 compounds such as ethylene, ethanol, and acetate.[17,18] Among these artificially photosynthesized C2 compounds, acetate is a promising product, because it is assimilated as a carbon and energy source for edible crops.[19] In addition, acetate can be converted to glucose using genetically modified yeasts.[20] These approaches are attracting attention because they can convert solar energy into food more efficiently than natural photosynthesis in crops. However, EC production of acetate from CO_2 using Cu-based catalysts powered by solar cells suffers from low faradaic efficiencies (FEs) of around 50% at most.[17–19]

In contrast, $CuFeO_2$, a p-type semiconducting ternary CuFe oxide, is a promising catalyst for photoelectrochemical (PEC) production of acetate, which could simplify the artificial-photosynthetic system compared with the combination of EC reactors and solar cells. The previously reported conduction-band minimum (CBM) ranges from −0.3 V to −0.8 V *vs.* reversible hydrogen electrode potential (RHE),[21–25] which is more negative than the reduction potential for acetate production from CO_2 (+0.1 V *vs.* RHE).[26] Therefore, $CuFeO_2$ has the ability for PEC production of acetate. In addition, its bandgap (E_g) of 1.5 eV is suitable to efficiently absorb solar energy.[25] Indeed, $CuFeO_2$-based photocathodes have demonstrated FEs of 69–80% for acetate production, which are exceptionally high values compared with other EC and PEC production of C2 compounds.[27,28] The presence of Fe adjacent to Cu promotes

Toyota Central R&D Labs., Inc., Nagakute, Aichi 480-1192, Japan

This journal is © The Royal Society of Chemistry 2025

Open Access Article. Published on 31 October 2025. Downloaded on 6/15/2026 3:06:40 AM. This article is licensed under a Creative Commons Attribution-NonCommercial 3.0 Unported Licence.

acetate production over other compounds.[27] However, these photocathodes suffer from low stability; the reduction current decreases significantly along with the leaching of Fe into the electrolytes within around 10 min after the PEC operation starts.[27]

To solve this problem, we investigated the PEC characteristics of CuFe oxides other than $CuFeO_2$. We focused on $CuFe_2O_4$, another p-type semiconducting ternary CuFe oxide, which has also been utilized for EC and PEC CO_2 reduction.[29–31] The oxidation state of Cu is Cu(II), which is more stable in general than Cu(I) contained in $CuFeO_2$,[32] offering potentially higher stability. In addition, $CuFe_2O_4$ could possess higher FEs for acetate production. Its CBM of −0.3 V *vs.* RHE is more positive than that of $CuFeO_2$,[25] and closer to the reduction potential for acetate production.[26] As a result, side reactions producing hydrogen, carbon monoxide, formate, and ethylene can be suppressed, leading to further higher FEs. Another point is the introduction of CuO into the CuFe oxides. Although a mixture of $CuFeO_2$ and CuO was used as the catalyst in a previous study,[27] the effect of introducing CuO has not yet been elucidated. Thus, we fabricated photocathodes using four kinds of catalysts: $CuFeO_2$, $CuFe_2O_4$, and these oxides mixed with CuO, and compared their PEC properties, to clarify the role of each constituent for realizing highly stable and highly selective acetate production.

2. Experimental

2.1 Fabrication of photocathodes using CuFe oxide catalysts

$CuFeO_2$ catalyst powder was synthesized by hydrothermal reaction according to a previously reported procedure.[33] CuI (2.8 mmol) and $FeCl_3$ (2.8 mmol) were dissolved in ultrapure water (electrical resistivity 18 MΩ cm, 14 mL) and nitrogen gas was bubbled through it for 30 min before use. Next, KOH (222 mmol) was added and further nitrogen gas was bubbled through it for 15 min. An exothermic reaction among the raw materials and KOH produced a dark-brown slurry. The obtained slurry was heated in an oven at 150 °C for 24 h. Then, the by-product salt (KCl) was removed by vacuum filtration of a mixture of the slurry and ultrapure water using a porous alumina filter (pore size 200 nm). Finally, the retentate was dried and pulverized using a mortar.

The $CuFeO_2$-loaded photocathodes were fabricated by dropping a slurry of the catalyst powder onto Ti substrates, followed by heat treatments. 20 mg of the powder was mixed with 2-propanol (2 mL) and subjected to ultrasonic homogenization (Biorepter, BR-II) in 30-second on and 30-second off cycles, repeated 30 times. Masking tape was applied to the four sides of a 25-mm-square Ti substrate of 0.5 mm in thickness to define the loading area of 15 mm square. Then, the slurry was dropped onto the exposed Ti surface, followed by a vacuum drying at room temperature. These processes of dropping and drying for the deposition were repeated 15 times for loading 2.7 mg cm^{-2} of the catalyst. After drying for 10 minutes at 100 °C, a heat treatment was finally carried out at 500 °C for 1 h. The photocathodes using the other catalysts were fabricated in the same manner, unless otherwise stated.

The $CuFeO_2$–CuO photocathodes were fabricated using a sequential process similar to that for the $CuFeO_2$ photocathodes, except that the raw materials were hydrothermally reacted at a lower temperature of 130 °C.[34]

The $CuFe_2O_4$–CuO photocathodes were fabricated by changing both temperatures for the hydrothermal synthesis and post-heat treatment. According to the phase diagram of CuFe oxide, a mixture of $CuFe_2O_4$ and CuO is more stable than $CuFeO_2$ below 1000 °C.[35] Therefore, the synthesized powder was heat-treated at 650 °C after being deposited on the Ti substrate to promote the phase separation into $CuFe_2O_4$ and CuO. For this purpose, the hydrothermal synthesis was carried out at a further lower temperature of 120 °C, which could destabilize the synthesized powder.

Meanwhile, $CuFe_2O_4$ catalyst powder was synthesized by the citric acid polymerization process.[36] Citric acid monohydrate (120 mmol) was dissolved in water (300 mL) at 60 °C. Next, $CuCO_3 \cdot Cu(OH)_2$ (15 mmol) and $FeC_6H_5O_7 \cdot nH_2O$ (60 mmol) were added and stirred for 1 h. Then, the water was evaporated using a hot stirrer at 100 °C for 2 h to obtain a precursor gel. The gel was calcined in an oven at 350 °C for 5 h, followed by firing in air at 800 °C for 12 h using an electric furnace. The product was ground using a tumbling ball mill to obtain fine $CuFe_2O_4$ powder.

2.2 Characterization of the synthesized catalysts and fabricated photocathodes

X-ray diffraction (XRD) measurements were carried out on the as-synthesized powders and photocathodes using an XRD instrument (Rigaku, Ultima IV). The fluorescence X-ray reduction mode was applied with a Cu Kα X-ray source operated at 40 kV and 40 mA. The θ–2θ method was adopted at a scan speed of 10° min^{-1}. The diffraction patterns were analysed using software (MDI, JADE Pro/Standard) for identification of the crystal structures. The particle morphologies and compositions of the photocathodes were analysed by field-emission scanning electron microscopy and energy dispersive X-ray spectroscopy (FE-SEM and EDX; Hitachi High-Tech, SU7000). The compositions of the catalysts were quantified by inductively coupled plasma optical emission spectroscopy (ICP-OES; Agilent Technology, ICP-OES 8900).

To derive the valence band maxima (VBMs) of the CuFe oxide catalysts and the CuO additive, ionization potentials (I_p) were evaluated by photoelectron yield spectroscopy (Bunko Keiki, BIP-KV201). Diffuse reflectance spectra were also measured using a spectrophotometer (Shimadzu, UV-3600i Plus) for evaluating E_g. From I_p and E_g, alignments of the conduction band minima (CBMs) relative to the reduction potentials of CO_2 to produce acetate and other compounds were determined.

The XRD and FE-SEM analyses were conducted again after the PEC operations to clarify the changes in the crystal structures and particle morphologies. To evaluate the leaching of the constituent elements during the PEC operations, Cu and Fe ions dissolved in the electrolytes were quantified by ICP-OES after the PEC operations.

Open Access Article. Published on 31 October 2025. Downloaded on 6/15/2026 3:06:40 AM. This article is licensed under a Creative Commons Attribution-NonCommercial 3.0 Unported Licence.

2.3 Evaluation of PEC reactions

The PEC reactions of the photocathodes were evaluated using a three-electrode reactor with an illumination window (EC Frontier, VB1300), shown in Fig. S1, a potentiostat (Biologic, VMP3), and a solar simulator equipped with a xenon lamp (Asahi Spectroscopy, HAL-C100). The photocathode was used as a working electrode (WE), with a Pt counter electrode (CE) and an Hg/Hg_2SO_4 reference electrode (RE). An ion-exchange membrane (DuPont, Nafion® N117) was inserted between the WE and the CE, and both sides were filled with an electrolyte of a 0.4 M potassium phosphate buffer aqueous solution (a mixture of 0.4 M K_2HPO_4 and 0.4 M KH_2PO_4 in a 1:1 volume ratio, 60 mL in total). CO_2 gas (100%) was bubbled into the electrolyte in the WE side. The reactor was illuminated by the solar simulator at 100 mW cm^{-2} (1 sun).

The photoresponse of the cathodes was evaluated by chopped-light linear sweep voltammetry (LSV), with the potential scanned from +0.7 V to −0.2 V *vs.* RHE at 2 mV sec^{-1}. Chopped-light current–time (*i–t*) measurements were also performed at a constant potential of +0.13 V *vs.* RHE.

i–t measurements under continuous illumination of 1 sun were conducted at +0.13 V *vs.* RHE for 1 h and 5 h for evaluations of the reaction selectivity and stability. During and after the *i–t* measurements, the concentrations of the produced acetate and formate ions dissolved in the electrolytes were quantified using an ion chromatograph (ThermoFisher Scientific, Integrion RFIC). The calibration curves were obtained using acetate and formate aqueous solutions of different concentrations (0.001, 0.01, 0.02, and 0.03 mM) prior to every measurement (see Fig. S2). The accuracy of the measured values was ±5%. According to eqn (1) and (2) describing the CO_2-reduction reactions, the FEs of the acetate production and formate production were calculated using eqn (3) and (4), respectively,

$$2CO_2 + 8H^+ + 8e^- \rightarrow CH_3COOH + 2H_2O \quad (1)$$

$$CO_2 + 2H^+ + 2e^- \rightarrow HCOOH \quad (2)$$

$$\text{Acetate FE} = A_a \times 8/(C/F) \times 100\ (\%) \quad (3)$$

$$\text{Formate FE} = A_f \times 2/(C/F) \times 100\ (\%) \quad (4)$$

where A_a and A_f are the amounts of the produced acetate and formate (mol), respectively, C is the total charge (C), and F is the Faraday constant (96485.3 C mol^{-1}).

The electrochemical impedance spectra (EIS) were acquired under illumination at +0.13 V *vs.* RHE, with an ac voltage of 10 mV and a frequency range from 10 mHz to 1 MHz for clarifying the roles of the CuFe oxide catalysts and the CuO additive.

In addition to the detailed evaluations using the three-electrode reactor described above, the photocathodes were combined with transparent anodes for assembling two-electrode reactors, as illustrated in Fig. S3, which would be a practical implementation. The photocathode was faced with an IrO_x/F-doped SnO_2/glass anode,[37] with a gap of 10 mm across an ion exchange membrane. Voltage–time (*v–t*) measurements were carried out at a constant current density of 0.2 mA cm^{-2} for 1 h under continuous illumination onto the photocathode through the transparent anode, and the results were compared with those in the dark.

2.4 *Operando* analyses of the oxidation states in the photocathodes

Operando X-ray absorption fine structure (XAFS) analyses were conducted at BL33XU of SPring-8 to clarify the oxidation states of Cu and Fe in the photocathodes during the PEC operations. The X-rays were incident from the rear face of the photocathode fabricated using a 5-μm-thick Ti substrate to eliminate the strong absorption by the potassium-containing electrolyte, and the fluorescence signals were detected. On the other hand, the transmission method was adopted for measurements on the standard samples of metal Cu, Fe, and oxides. The details of the experimental set-up are described in the SI and Fig. S4.

First, the XAFS measurement was carried out on the photocathode in air in the dark. Next, the reactor was filled with the CO_2-bubbled electrolyte, and the XAFS spectra at the Cu K-edge and Fe K-edge were acquired at the open-circuit voltage (OCV) in the dark. Then, *i–t* operations at a constant potential of +0.13 V *vs.* RHE were conducted sequentially under illumination, in the dark, and under illumination again. At the OCV and during these *i–t* operations, the XAFS measurements were repeated at a rate of 50 s per spectrum with an additional 10 s for setting, *i.e.*, every 60 s. The measured XAFS spectra were converted to Fourier-transformed extended X-ray absorption fine structure (FT-EXAFS) spectra.

3. Results and discussion

3.1 Crystal structures of the photocathode catalysts

Fig. 1 shows the XRD patterns and appearance of the $CuFeO_2$-based photocathodes. Both exhibited a similar appearance of dark gray. However, the compositions of these two photocathodes were different from each other. Only the diffraction peaks

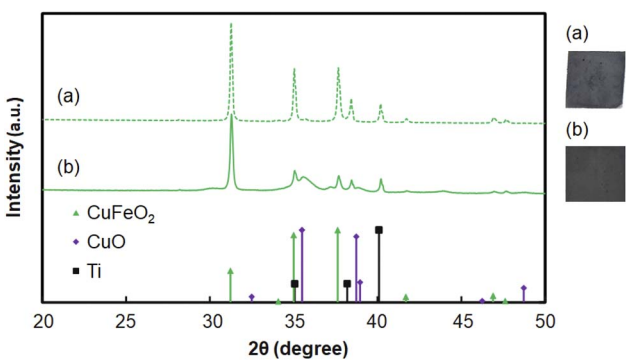

Fig. 1 XRD patterns and appearance of (a) the $CuFeO_2$ photocathode fabricated by the hydrothermal synthesis at 150 °C followed by the heat treatment at 500 °C, and (b) the $CuFeO_2$–CuO photocathode hydrothermally synthesized at 130 °C, followed by the heat treatment at 500 °C. Reference PDF data of $CuFeO_2$, CuO, and Ti are also indicated.

 This journal is © The Royal Society of Chemistry 2025

Open Access Article. Published on 31 October 2025. Downloaded on 6/15/2026 3:06:40 AM.
This article is licensed under a Creative Commons Attribution-NonCommercial 3.0 Unported Licence.

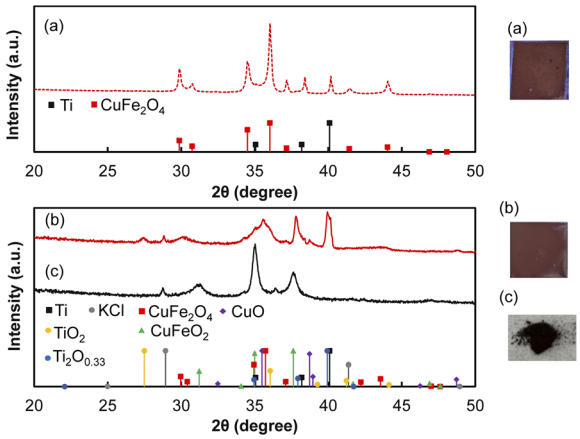

Fig. 2 XRD patterns and appearance of (a) the $CuFe_2O_4$ photocathode fabricated by the citric acid polymerization at 800 °C, (b) the $CuFe_2O_4$–CuO photocathode fabricated by the hydrothermal synthesis at 120 °C followed by the heat treatment at 650 °C, and (c) the as-synthesized powder at 120 °C. Reference PDF data of $CuFe_2O_4$, CuO, $CuFeO_2$, Ti, TiO_2 and KCl are also indicated.

attributed to hexagonal $CuFeO_2$ (PDF #04-009-4371, ref. 38) appeared in the pattern of the $CuFeO_2$ photocathode fabricated by the hydrothermal synthesis at 150 °C. The Fe/Cu atomic ratio was 1.07. By contrast, broad peaks centered at $2\theta = 35.5°$ and 38.7° were exhibited when the hydrothermal synthesis was carried out at 130 °C, indicating the presence of monoclinic CuO (PDF #00-045-0937, ref. 39). Nevertheless, the Fe/Cu atomic ratio was 1.02, suggesting the presence of a small amount of amorphous Fe oxides that was not detected by XRD.

The XRD patterns of the $CuFe_2O_4$ and $CuFe_2O_4$–CuO photocathodes are compared in Fig. 2. All the diffraction peaks were attributed to tetragonal $CuFe_2O_4$ (PDF #04-006-5656, ref. 40) for the reddish-brown-coloured $CuFe_2O_4$ photocathode, although the composition was slightly Fe-rich; the Fe/Cu ratio was 2.20. On the other hand, broad peaks originating from monoclinic CuO appeared in addition to the tetragonal $CuFe_2O_4$ signals (PDF#04-007-5165, ref. 41) for the $CuFe_2O_4$–CuO photocathode fabricated by the hydrothermal synthesis at 120 °C followed by the heat treatment at 650 °C, with no trace of $CuFeO_2$. The presence of CuO is consistent with the Fe/Cu atomic ratio of 1.75. This XRD pattern is significantly different from that of the as-synthesized powder composed of hexagonal $CuFeO_2$. These results clarify the phase separation by the high-temperature treatment at 650 °C, accompanied by colour change from dark gray to reddish brown. On the other hand, the diffraction peaks observed at 27.5° and 28.9° were attributed to TiO_2 and KCl, respectively, which are inert to the CO_2 reduction reactions. The former was generated by oxidation of the Ti substrate during the high-temperature process, while the latter was a residual by-product from the $CuFeO_2$ synthesis that remained after washing.

3.2 PEC characteristics of the photocathodes

Fig. 3 shows the *i*–*t* curves of the three-electrode reactors using the four kinds of photocathodes under continuous 1 sun

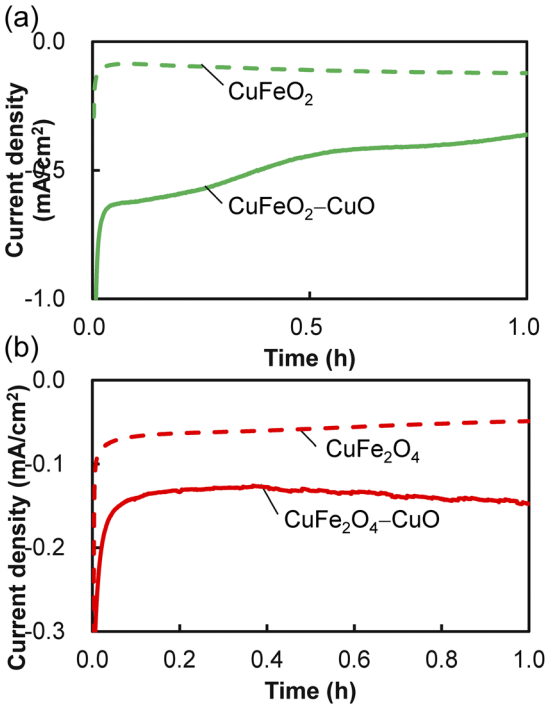

Fig. 3 *i*–*t* curves of the three-electrode reactors under continuous illumination at a constant potential of +0.13 V *vs.* RHE using (a) the $CuFeO_2$-based photocathodes and (b) the $CuFe_2O_4$-based photocathodes. Note that the ranges of the current density are different between the two figures.

illumination. The potential was set at +0.13 V *vs.* RHE, which is slightly more positive than the reduction potential for acetate production from CO_2 (+0.098 V *vs.* RHE).[26] Existence of a photoresponse, *i.e.*, an increase in the current densities by illumination at this potential, was confirmed (see Fig. S5). The magnitudes of the current densities of the $CuFeO_2$ and $CuFe_2O_4$ photocathodes were smaller than 0.1 mA cm^{-2}. On the other hand, they were notably increased by the introduction of CuO. In particular, the effect is more notable for the $CuFeO_2$-based photocathode. However, the current density of the $CuFeO_2$–CuO photocathode gradually decreased in magnitude during the 1 h operation, in contrast to the slowly increasing current density without CuO. This is due to the reduction of the Cu species to Cu (0) in the catalyst, as described later. By contrast, the $CuFe_2O_4$–CuO photocathode maintained a stable current density higher than those of the $CuFeO_2$ and $CuFe_2O_4$ photocathodes. Thus, the $CuFe_2O_4$–CuO photocathode realized stable PEC operation.

Furthermore, both $CuFe_2O_4$-based photocathodes achieved high FEs of acetate production exceeding 90%, as summarized in Table 1. Thus, the acetate FE has been notably improved from the present values and previously reported values of up to 80% using $CuFeO_2$-based photocathodes,[27,28] although the impact of the possible Fe oxide in the present $CuFeO_2$–CuO photocathode has not yet been clarified.

The significant point is that the introduction of CuO into $CuFe_2O_4$ increased the current density in magnitude while maintaining the high acetate FE. The mechanism underlying

Open Access Article. Published on 31 October 2025. Downloaded on 6/15/2026 3:06:40 AM. This article is licensed under a Creative Commons Attribution-NonCommercial 3.0 Unported Licence.

Table 1 Magnitudes of the average current densities (I_{av}), rates and FEs for acetate and formate production during the 1 h PEC operations of the three-electrode reactors using the $CuFeO_2$, $CuFeO_2$–CuO, $CuFe_2O_4$, and $CuFe_2O_4$–CuO photocathodes. Average values for two or three samples are tabulated. The rates and FEs include an additional 5% (relative) measurement error. The deviations represent the differences between the maximum and minimum values, which are particularly large for formate production due to the low formate concentrations in the electrolytes

Photocathode	Powder synthesis temp. and time	Post heating temp. (°C)	I_{av} (mA cm^{-2})	Acetate production rate (μmol h^{-1})	Acetate FE (%)	Formate production rate (μmol h^{-1})	Formate FE (%)
$CuFeO_2$	150 °C 24 h	500	0.11 ± 0.02	0.30 ± 0.06	59 ± 1.3	0.12 ± 0.01	6 ± 0.2
$CuFeO_2$–CuO	130 °C 24 h	500	0.43 ± 0.02	1.60 ± 0.05	79 ± 2.3	0.24 ± 0.03	3 ± 0.4
$CuFe_2O_4$	350 °C 5 h + 800 °C 12 h	500	0.059 ± 0.01	0.25 ± 0.04	92 ± 1.0	0.09 ± 0.05	8 ± 2.4
$CuFe_2O_4$–CuO	120 °C 24 h	600	0.18 ± 0.01	0.78 ± 0.02	92 ± 1.4	0.36 ± 0.12	11 ± 3.4

these great features is discussed in Section 3.5. Consequently, the $CuFe_2O_4$-based photocathode is promising for highly efficient artificial-photosynthetic acetate production from CO_2.

Next, the $CuFe_2O_4$–CuO photocathode was applied to the two-electrode reactor using the IrO_x-based transparent anode, which would be a practical implementation. Fig. 4(a) compares two v–t characteristics at a constant current density of 0.2 mA cm^{-2} measured under continuous illumination and in the dark. The voltage under continuous illumination was lower than that in the dark, even at the initial stage of the measurements. The gradual decrease in the voltage would be due to temperature elevation associated with the illumination. The oscillation was likely caused by the pulsatile flow of the electrolyte.

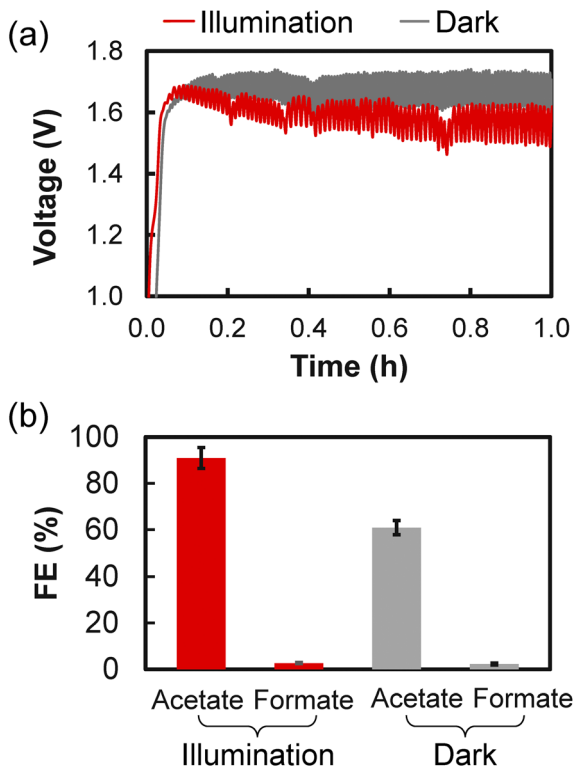

Fig. 4 (a) v–t characteristics of the two-electrode reactors composed of the $CuFe_2O_4$–CuO photocathode and IrO_x-based transparent anode at a constant current density of 0.2 mA cm^{-2}. (b) FEs of acetate and formate production. The error bars represent the differences between the maximum and minimum values among the two samples.

Another, and more significant, effect of illumination is the notable increase in the FE for acetate production, as is clear from Fig. 4(b). The acetate FE as high as that for the three-electrode reactors, exceeding 90% with stable operation, suggests the promising feature of the $CuFe_2O_4$-based photocathode toward practical use.

3.3 Changes in the photocathodes induced by the PEC operations

To clarify the reasons for the notable difference in the stabilities during the PEC operations between the four kinds of photocathodes, we compared the XRD patterns measured after the PEC operations for 1 h with those before the operations.

As shown in Fig. 5(a) and (b), the diffraction peaks of metallic Cu appeared for the $CuFeO_2$-based photocathodes after the PEC operations, suggesting that some of the Cu species were reduced to Cu(0). In particular, the presence of the Cu peak was more notable when CuO was introduced, accompanied by apparent decreases in the $CuFeO_2$ signals. This would be the cause of the decrease in the current density, in short, the low stability of the $CuFeO_2$–CuO photocathode shown in Fig. 3(a).

By contrast, metal Cu peaks were not observed even after the PEC operations for the $CuFe_2O_4$-based photocathodes, as is clear from Fig. 5(c) and (d), or no other significant changes. In short, Cu reduction during the PEC operation was sufficiently suppressed in these photocathodes, leading to the stable operation displayed in Fig. 3(b).

We further evaluated the stability of these photocathodes by quantifying the Cu and Fe species dissolved in the electrolytes after the PEC operations for 1 h. Table 2 indicates that large amounts of Cu and Fe were leached from the $CuFeO_2$-based photocathode into the electrolyte. By contrast, the leaching was significantly suppressed for the $CuFe_2O_4$-based photocathode. The mechanism underlying the higher stability of $CuFe_2O_4$ than $CuFeO_2$ has not yet been fully elucidated. In general, divalent Cu oxides are more stable in aqueous electrolytes than monovalent Cu oxides,[32] since the redox potentials of Cu^{2+}/Cu^{1+} (+0.15 V *vs.* RHE), Cu^{2+}/Cu^0 (+0.34 V *vs.* RHE), and Cu^{1+}/Cu^0 (+0.52 V *vs.* RHE)[42] are all more positive than the applied potential of +0.13 V *vs.* RHE in increasing order, and consequently, Cu^{1+} is reduced more easily than Cu^{2+}.

To clarify these changes induced by the PEC operations, we performed a longer operation test for 5 h. As shown in Fig. S6,

 This journal is © The Royal Society of Chemistry 2025

Open Access Article. Published on 31 October 2025. Downloaded on 6/15/2026 3:06:40 AM.
This article is licensed under a Creative Commons Attribution-NonCommercial 3.0 Unported Licence.

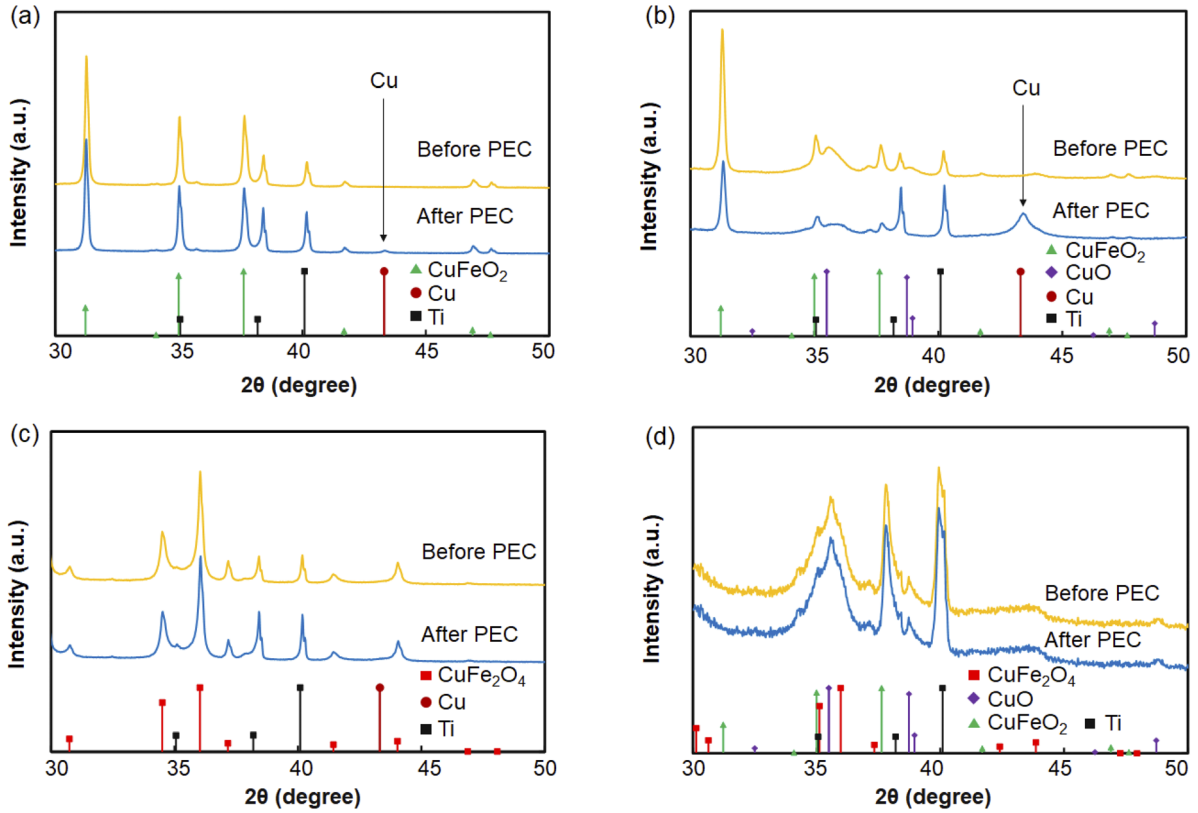

Fig. 5 XRD patterns of the photocathodes before and after the *i*–*t* measurements under continuous illumination for 1 h at a constant potential of +0.13 V *vs.* RHE: (a) $CuFeO_2$, (b) $CuFeO_2$–CuO, (c) $CuFe_2O_4$, and (d) $CuFe_2O_4$–CuO. Reference PDF data of $CuFeO_2$, $CuFe_2O_4$, CuO, Cu, and Ti are also indicated.

Table 2 Cu and Fe amounts leached into the electrolytes measured after the *i*–*t* measurements under continuous illumination for 1 h at a constant potential of +0.13 V *vs.* RHE. The concentrations in the electrolytes (in μg mL^{-1}) are converted to the ratios (in %) of the amounts leached into the electrolyte to those contained in the photocathodes before the *i*–*t* measurements

Photocathode	Cu (μg mL^{-1})	Cu (%)	Fe (μg mL^{-1})	Fe (%)
$CuFeO_2$–CuO	2.6	6.9	12	36
$CuFe_2O_4$–CuO	0.01	0.04	0.75	1.8

the current densities of the $CuFeO_2$-based photocathode decreased over time. By contrast, the $CuFe_2O_4$ photocathode exhibited stable operation for 5 h. However, the current density gradually increased when CuO was introduced; the reason has not yet been elucidated. Fig. S7 depicts the acetate-production performance. The amount of acetate produced by the $CuFe_2O_4$ photocathode increased linearly with operation time. This leads to the maintenance of the acetate production rate and FE exceeding 90% over 5 h. However, the rate and FE for the $CuFe_2O_4$–CuO photocathode decreased after 3 h, in common with the $CuFeO_2$-based photocathodes, indicating degradation of these three photoelectrodes.

XRD patterns measured after the 5 h operation, shown in Fig. S8, indicated further structural changes. The weak peak of metallic Cu observed after 1 h increased, accompanied by a notable decrease in the $CuFeO_2$ peak for the $CuFeO_2$ photocathode. This suggests that decomposition of $CuFeO_2$ proceeded, resulting in the decreasing current density. The metal Cu peak also appeared for the $CuFe_2O_4$–CuO photocathode, although it was not detected after 1 h. On the other hand, the intensity of the $CuFe_2O_4$ peak remained almost unchanged. The XRD pattern of the $CuFe_2O_4$ photocathode remained unchanged.

Notable changes were also observed in the morphology for the $CuFeO_2$-based photocathodes, as is clear from the FE-SEM images and EDX mappings in Fig. S9 and S10. Most of the plate-like $CuFeO_2$ particles of a few micrometers in size observed before the PEC operation were transformed into spherical metal Cu particles. The Fe concentrations significantly decreased, as already evidenced by the composition analyses of the electrolytes after the 1 h PEC operation.

By contrast, no significant changes in the morphology or composition were exhibited for the $CuFe_2O_4$ photocathode (see Fig. S11). This, along with the XRD result, supports its high stability during the 5 h operation.

The fine CuO particles in the $CuFe_2O_4$–CuO photocathode observed before the PEC operation disappeared after 5 h, as displayed in Fig. S12. Instead, spherical metallic Cu particles appeared. On the other hand, the Fe/Cu atomic ratio equalled approximately 2 in the area where the metal Cu particles were not observed, indicating the existence of $CuFe_2O_4$. These results

Open Access Article. Published on 31 October 2025. Downloaded on 6/15/2026 3:06:40 AM. This article is licensed under a Creative Commons Attribution-NonCommercial 3.0 Unported Licence.

are consistent with the XRD patterns after 5 h. Consequently, it was suggested that $CuFe_2O_4$ is stable regardless of the existence of CuO, and that the degradation of the $CuFe_2O_4$–CuO photocathode was due to the reduction of the CuO particles to metallic Cu.

3.4 *Operando* XAFS analyses of the $CuFeO_2$–CuO and $CuFe_2O_4$–CuO photocathodes

To clarify the changes in the photocathodes while the PEC operations are ongoing, we conducted *operando* XAFS measurements. For this purpose, the catalyst layers must be sufficiently thin so that the fluorescence spectra are not distorted by reabsorption of the fluorescence X-rays. Prior to the XAFS measurements, it was confirmed that when the loading amount of the catalyst is decreased to one-tenth of the original (2.7 mg cm^{-2}), the reabsorption of the fluorescence X-rays is negligibly weak while the acetate FE is as high as that for the original amount. Therefore, the loading amount of 0.27 mg cm^{-2} was adopted for the XAFS measurements. The PEC performances of the photocathodes using the thin $CuFe_2O_4$–CuO layers are depicted in Fig. S13.

Fig. 6(a) shows the X-ray absorption near edge structure (XANES) spectra at the Cu K-edge for the $CuFeO_2$–CuO photocathode measured sequentially under different conditions: at the OCV in the dark, and during the operations at a constant potential of +0.13 V *vs.* RHE under illumination, in the dark, and under illumination again.

At the OCV, the absorption edge of the Cu K-edge spectrum coincided with that of Cu_2O, exhibiting no changes from those in air, as shown in Fig. S14(a). This indicates that the oxidation state of most of the Cu species was Cu(I).

During the sequential operations, the intensity of the main peak located at around 9000 eV in the Cu K-edge spectra gradually decreased. Therefore, for clarifying the changes in the oxidation state of the Cu species, the spectrum at each cycle was decomposed into four spectra: the spectrum of the photocathode measured at the OCV before the operation ("before") and additional spectra of the CuO, Cu_2O, and Cu standard samples by the linear least squares fitting. Fig. S16 indicates that the ratio of "before" decreased, whereas that of Cu increased as the operation proceeded, suggesting that a considerable fraction of the Cu species was reduced to Cu(0) during the operations.

The formation of Cu(0) was supported by converting the XAFS spectra to the FT-EXAFS spectra depicted in Fig. 6(b). The FT magnitude at around $R = 2.0$ Å, corresponding to the Cu atoms as the first nearest neighbours of Cu in metal Cu, gradually increased during the operations, although it was negligibly small in the "before" state. Fig. 6(c) compares the FT-EXAFS spectra of the "before" and the final stage of the second illumination ("final") with those of the standard samples. In the "final" spectrum, the peak originating from metallic Cu appeared at around $R = 2.0$ Å, although it was not exhibited in the "before" spectrum. It should be noted that the observed peak position was shifted from that for the standard sample of metal Cu ($R = 2.2$ Å), because of interference with the signals originating from phases other than metallic Cu.

On the other hand, the Fe K-edge spectra scarcely changed throughout the measurements, as depicted in Fig. S14(b) and S15(a), indicating that the oxidation state of the Fe species was always Fe(III).

These results of the operand XAFS analyses agree with the XRD results shown in Fig. 5(b). Thus, the reduction of the Cu

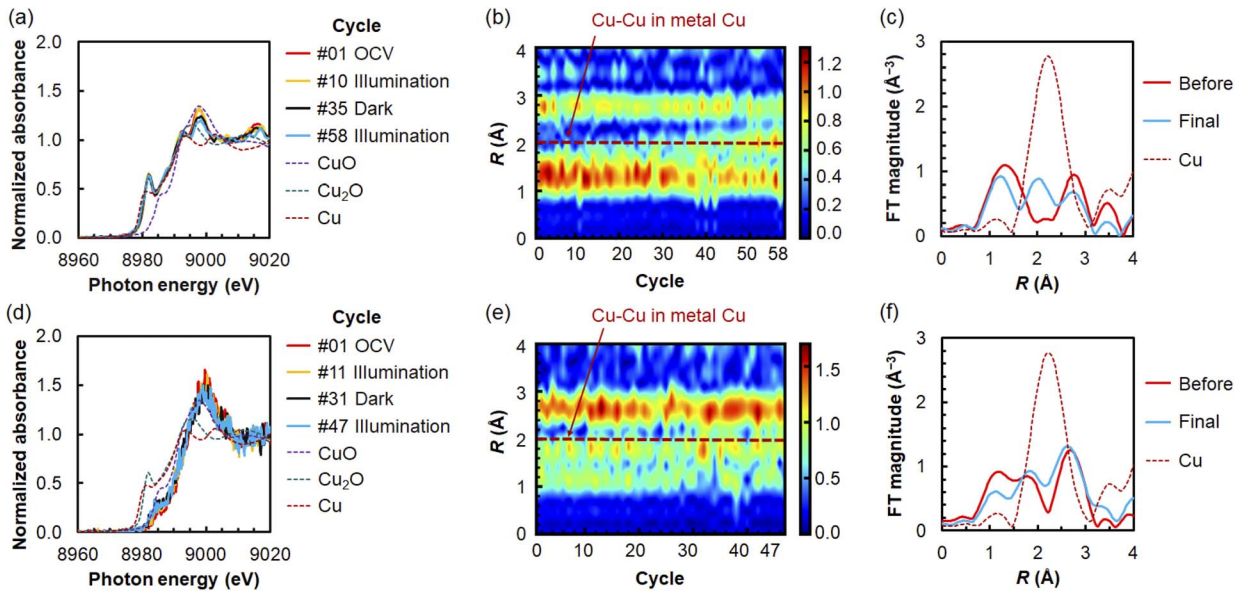

Fig. 6 Changes in (a) the Cu K-edge XANES spectra and (b) FT-EXAFS spectra of the $CuFeO_2$–CuO photocathode during the operations. The measurements were sequentially conducted as follows: at the OCV in the dark (Cycle 1–3), and operations at a constant potential of +0.13 V *vs.* RHE under illumination (Cycle 4–33), in the dark (Cycle 34–48), and under illumination (Cycle 49–58). (c) The FT-EXAFS spectra at the OCV before the operation ("before", average over Cycle 1–3) and at the final stage of the second illumination ("final", average over the last 3 cycles). (d)–(f) Results for the $CuFe_2O_4$–CuO photocathode measured at OCV (Cycle 1–2), under illumination (Cycle 3–18), in the dark (Cycle 19–36), and under illumination (Cycle 37–47).

 This journal is © The Royal Society of Chemistry 2025

Open Access Article. Published on 31 October 2025. Downloaded on 6/15/2026 3:06:40 AM.
This article is licensed under a Creative Commons Attribution-NonCommercial 3.0 Unported Licence.

species would be the cause of the gradual decrease in the current density, in other words, low stability during the PEC operation depicted in Fig. 3(a).

By contrast, the results for the $CuFe_2O_4$–CuO photocathode exhibited no apparent changes in the oxidation states of the Cu or Fe species. Fig. 6(d) shows the Cu K-edge XANES spectra, indicating that the "before" oxidation state of the Cu species was Cu(II), just like that in the air shown in Fig. S14(c), and remained unchanged during the sequential operations, as is clear from Fig. 6(e) and (f). The oxidation state of the Fe species was always Fe(III) (see Fig. S14(d) and S15(b)). These results support the highly stable operation displayed in Fig. 3(b).

3.5 Role of each constituent in the $CuFe_2O_4$–CuO photocathode for PEC production of acetate

The newly developed photocathode using the $CuFe_2O_4$-based catalyst achieved high stability along with a high acetate FE exceeding 90% during 1 h of PEC operation. Another significance is that the introduction of CuO into $CuFe_2O_4$ approximately doubled the current density and the acetate production rate. Thus, we further investigated this photocathode to clarify the origins of these great features.

The high acetate FE was also realized using the $CuFe_2O_4$ photocathode, as shown in Table 1. Therefore, $CuFe_2O_4$ guarantees the high selectivity of acetate production. The origin of this high selectivity is discussed later.

On the other hand, the photocurrent density and acetate production rate were doubled by introducing CuO. To elucidate the role of CuO, EIS measurements were carried out. Fig. 7 compares the Nyquist plots of the $CuFe_2O_4$–CuO photocathode with those of the $CuFe_2O_4$ photocathode measured under illumination and in the dark at the same DC bias (+0.13 V *vs.* RHE) adopted for the *i*–*t* measurements. These results are interpreted using the equivalent circuit composed of three resistances (R_1–R_3) and two capacitances (C_2 and C_3) illustrated in Fig. 7(c).[43] R_1 originates from the charge transfer at the interface between the catalyst layer and Ti substrate, R_2 and C_2 from the charge transport in the porous catalyst layer, and R_3 and C_3 from the charge transfer across the photocathode/electrolyte interface.

The introduction of CuO notably decreased R_2, although R_1 remained unchanged, owing to the function of CuO as a conductive additive. This contributed to the doubled photocurrent density and acetate production rate at a constant potential. In addition, R_2 was smaller under illumination. This is exactly the origin of the lower voltage under illumination during the *v*–*t* measurements depicted in Fig. 4 and the photoresponse displayed in Fig. S5. Although R_3 provides information on the reaction activities and selectivity, accurate values were not derived because of distorted semicircles and low S/N ratios.

Finally, to clarify the electron-transfer pathways, the energy levels of the constituents were determined by measuring the photoelectron yield spectra and diffuse reflectance spectra. The measured results are shown in Fig. S17 and S18 with the I_p and E_g values derived from the spectra, respectively.

The resultant energy levels are depicted in Fig. 8. Photoexcited electrons in $CuFe_2O_4$ reduce CO_2 to produce acetate. The CBM of $CuFe_2O_4$ is closer to the CO_2 reduction potential for acetate production than that of $CuFeO_2$. This suppresses side reactions producing hydrogen, formate, carbon monoxide, and

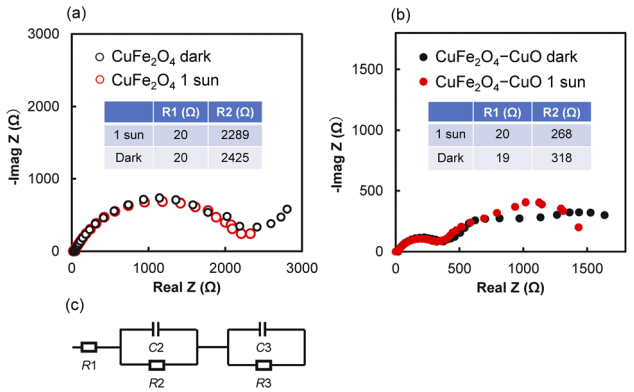

Fig. 7 Nyquist plots of the three-electrode reactors using the (a) $CuFe_2O_4$–CuO and (b) $CuFe_2O_4$ photocathodes measured at a DC bias of +0.13 V *vs.* RHE under 1 sun illumination and in the dark. The fitted values of R_1 and R_2 were indicated. (c) Equivalent circuit.

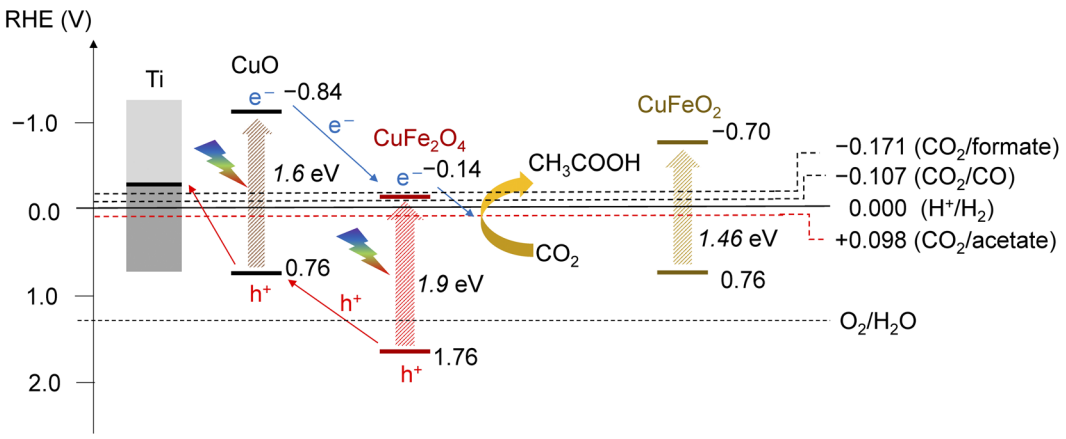

Fig. 8 Energy levels of CuO, $CuFe_2O_4$ and $CuFeO_2$ determined from the photoelectron yield spectra (Fig. S17) and diffuse reflectance spectra (Fig. S18), and electron and hole transfer pathways leading to acetate production from CO_2.

Open Access Article. Published on 31 October 2025. Downloaded on 6/15/2026 3:06:40 AM. This article is licensed under a Creative Commons Attribution-NonCommercial 3.0 Unported Licence.

ethylene more efficiently. Consequently, the higher FE exceeding 90% is achieved using the $CuFe_2O_4$ catalyst. On the other hand, the PEC reaction mechanism of acetate production by CO_2 reduction on CuFe oxide surfaces has not yet been fully elucidated. It has been proposed that CO_2 adsorbed on the Fe sites is preferentially reduced to *CO bound to the surfaces,[44] which subsequently reacts with water to form *COH under illumination, followed by C–C coupling with another *COH or with *CO to produce acetate.[45–47] Detailed analyses of the reaction mechanism could reveal other notable features of $CuFe_2O_4$ in addition to its appropriate CBM.

In addition, electrons photoexcited in CuO also contribute to acetate production after migrating into $CuFe_2O_4$, rather than reducing CO_2 on the CuO surfaces to produce other substances. Holes migrate to the Ti substrate directly or *via* CuO. Consequently, although the incident photons are partially absorbed by the conductive additive CuO, they are efficiently utilized for acetate production on the $CuFe_2O_4$ surfaces. This is the reason why the high acetate FE is maintained when CuO is introduced, and the current density is notably increased. However, long-term stability of CuO during the PEC operation was not sufficiently high, as discussed in Section 3.3. Therefore, replacement of CuO with a more stable conductive additive is needed. Combination with organic hole conductors would be a promising candidate to achieve both high current density and high stability, because the energy levels of these materials can be well adjusted to those of $CuFe_2O_4$ and relevant reactions by designing appropriate molecular structures.

4. Conclusions

We have fabricated photocathodes using a newly developed $CuFe_2O_4$-based catalyst for artificial photosynthesis and achieved highly stable and highly selective PEC production of acetate from CO_2. The FEs for acetate production exceeded 90%, with stable operation for 1 h. XRD, FE-SEM, EDX, and *operando* XAFS analyses revealed that there were no apparent changes in the $CuFe_2O_4$-based catalyst during the PEC operations. In contrast, a considerable fraction of the Cu species in the conventional $CuFeO_2$-based catalyst was reduced to Cu(0), while a significant portion of the Fe species was leached into the electrolyte, resulting in notable degradation in the PEC performance. It has been revealed that $CuFe_2O_4$ guarantees the high FE and high stability, while CuO functions as a conductive additive, leading to the improved current density while maintaining the high FE. However, the long-term stability of CuO was not sufficiently high for practical use; a more stable conductive additive is needed for fully exploiting the high stability and selectivity of $CuFe_2O_4$. The artificially photosynthesized acetate can be converted into edible products *via* bioprocesses, offering a potentially more efficient solar-energy conversion to food than natural photosynthesis in the near future.

Author contributions

N. K. and Y. T. conceived the concrete concept and designed the experiments. S. S. and N. K. synthesized the CuFe oxide powders and fabricated the photocathodes. N. K., S. S. and S. M. contributed to the characterization of the photocathodes. N. K. evaluated the PEC reactions. Y. F. N., N. K., and Y. T. conducted the *operando* XAFS experiments. Y. T. and S. M. supervised the project. All authors participated in the discussion.

Conflicts of interest

There are no conflicts to declare.

Data availability

The data supporting this article have been included as part of the supplementary information (SI). Supplementary Information is available. See DOI: **https://doi.org/10.1039/d5ta06122a**.

Acknowledgements

The authors are grateful to Natsumi Nojiri for designing the two-electrode reactors with the electrolyte-flow setup, Juntaro Seki for the FE-SEM analyses, and Dr Satoru Kosaka for the composition analyses. We also thank Dr Tsuyoshi Hamaguchi, Dr Nobuhiro Ogihara, and Dr Masaoki Iwasaki for their helpful comments and encouragement. The *operando* XAFS measurements were carried out at BL33XU of SPring-8 with the approval of the Japan Synchrotron Radiation Research Institute (JASRI) (Proposal No. 2024A7047 and 2024B7047).

References

1 S. Sato, T. Arai, T. Morikawa, K. Uemura, T. M. Suzuki, H. Tanaka and T. Kajino, *J. Am. Chem. Soc.*, 2011, **133**, 15240.
2 J. Marshall, *Nature*, 2014, **510**, 22.
3 T. Arai, S. Sato and T. Morikawa, *Energy Environ. Sci.*, 2015, **8**, 1998.
4 J. Wu, Y. Huang, W. Ye and Y. Li, *Adv. Sci.*, 2017, **4**, 1700194.
5 J. H. Kim, D. Hansora, P. Sharma, J. W. Jang and J. S. Lee, *Chem. Soc. Rev.*, 2019, **48**, 1908.
6 J. He and C. Janáky, *ACS Energy Lett.*, 2020, **5**, 1996.
7 T. Morikawa, S. Sato, K. Sekizawa, T. M. Suzuki and T. Arai, *Acc. Chem. Res.*, 2022, **55**, 933.
8 B. Tang and F.-X. Xiao, *ACS Catal.*, 2022, **12**, 9023.
9 G. Segev, J. Kibsgaard, C. Hahn, Z. J. Xu, W.-H. Cheng, T. G. Deutsch, C. Xiang, J. Z. Zang, L. Hammarström, D. G. Nocera, A. Z. Weber, P. Agbo, T. Hisatomi, F. E. Osterloh, K. Domen, F. F. Abdi, S. Haussener, D. J. Miller, S. Ardo, P. C. Mclntyre, T. Hannappel, S. Hu, H. Atwater, J. M Gregoire, M. Z. Ertem, L. D. Sahrp, K.-S. Choi, J. S. Lee, O. Ishitani, J. W. Ager, R. R. Prabhakar, A. T. Bell, S. W. Boettcher, K. Vincent, K. Takanabe, V. Artero, R. Napier, B. R. Cuenya, M. T. M. Kopper, R. V. D. Krol and F. Houle, *J. Phys. D: Appl. Phys.*, 2022, **55**, 323003.
10 Y. Takeda and T. Morikawa, *J. Phys. Energy*, 2025, **7**, 012002.
11 S. Chakraborty and S. C. Peter, *ACS Energy Lett.*, 2025, **10**, 2359.
12 A. R. A. Maragno, G. Cwicklinski, M. Matheron, R. Vanoorenberghe, J.-M. Borgard, A. Morozan, J. Fize,

 This journal is © The Royal Society of Chemistry 2025

Open Access Article. Published on 31 October 2025. Downloaded on 6/15/2026 3:06:40 AM. This article is licensed under a Creative Commons Attribution-NonCommercial 3.0 Unported Licence.

M. Pellat, C. Cavazza, V. Artero and S. Charton, *Joule*, 2024, **8**, 2325.
13 N. Kato, S. Mizuno, M. Shiozawa, N. Nojiri, Y. Kawai, K. Fukumoto, T. Morikawa and Y. Takeda, *Joule*, 2021, **5**, 687.
14 N. Kato, Y. Takeda, Y. Kawai, N. Nojiri, M. Shiozawa, S. Mizuno, K. Yamanaka, T. Morikawa and T. Hamaguchi, *ACS Sustain. Chem. Eng.*, 2021, **9**, 16031.
15 B. Liu, L. Ma, H. Feng, Y. Zhang, J. Duan, Y. Wang, D. Liu and Q. Li, *ACS Energy Lett.*, 2023, **8**, 981.
16 K. Sekizawa, S. Sato, N. Sakamoto, T. M. Suzuki and T. Morikawa, *ChemRxiv*, 2024, preprint, DOI: 10.26434/chemrxiv-2024-brj46.
17 K. P. Kuhl, E. R. Cave, D. N. Abram and T. F. Jaramillo, *Energy Environ. Sci.*, 2012, **5**, 7050.
18 S. Nitopi, E. Bertheussen, S. B. Scott, X. Liu, A. K. Engstfeld, S. Horch, B. Seger, I. E. L. Stephens, K. Chan, C. Hahn, J. K. Nørskov, T. F. Jaramillo and I. Chorkendorff, *Chem. Rev.*, 2019, **119**, 7610.
19 E. C. Hann, S. Overa, M. Harland-Dunaway, A. F. Narvaez, D. N. Le, M. L. Orozco-Cardenas, F. Jiao and R. E. Jinkerson, *Nat. Food*, 2022, **3**, 461.
20 T. Zheng, M. Zhang, L. Wu, S. Guo, X. Liu, J. Zhao, W. Xue, J. Li, C. Liu, X. Li, Q. Jiang, J. Bao, J. Zeng, T. Yu and C. Xia, *Nat. Catal.*, 2022, **5**, 388.
21 K. Sivula and R. V. D. Krol, *Nat. Rev. Mater.*, 2016, **1**, 15010.
22 K. Rajeshwar, M. K. Hossain, R. T. Macaluso, C. Janáky, A. Varga and P. J. Kulesza, *J. Electrochem. Soc.*, 2018, **165**, H3192.
23 J. Gu, A. Wuttig, J. W. Krizan, Y. Hu, Z. M. Detweiler, R. J. Cava and A. B. Bocarsly, *J. Phys. Chem. C*, 2013, **117**, 12415.
24 C. G. Read, Y. Park and K. S. Choi, *J. Phys. Chem. Lett.*, 2012, **3**, 1872.
25 I. L. E. Gonzaga and C. C. Mercado, *Rev. Adv. Mater. Sci.*, 2022, **61**, 437.
26 D. Li, K. Yang, J. Lian, J. Yan and S. F. Liu, *Adv. Energy Mater.*, 2022, **12**, 2201070.
27 X. Yang, E. A. Fugate, Y. Mueanngern and L. R. Baker, *ACS Catal.*, 2017, **7**, 177.
28 S.-H. Oh, H.-Y. Kang, W.-H. Joo and Y.-C. Joo, *ChemCatChem*, 2020, **12**, 5185.
29 K. M. R. Karim, H. R. Ong, H. Abdullah, A. Yousuf, C. K. Cheng and M. M. R. Khan, *Int. J. Hydrogen Energy*, 2018, **43**, 18185.
30 K. M. R. Karim, H. R. Ong, H. Abdullah, A. Yousuf, C. K. Cheng and M. M. R. Khan, *Bull. Chem. React. Eng. Catal.*, 2018, **13**, 236.
31 J. Zander, M. Weiss and R. Marchall, *Adv. Energy Sustain. Res.*, 2023, **4**, 2200184.
32 N. Zayyoun, L. Bahmad, L. Laanab and B. Jaber, *Appl. Phys. A*, 2016, **122**, 488.
33 Y. Jin and G. Chumanov, *RSC Adv.*, 2016, **6**, 26392.
34 D. Xiong, Y. Qi, X. Li, X. Liu, H. Tao, W. Chen and X. Zhao, *RSC Adv.*, 2015, **5**, 49280.
35 J. Schorne-Pinto, L. Cassayre, L. Presmanes and A. Barnabe, *Inorg. Chem.*, 2019, **58**, 6431.
36 M. Kakihana, *J. Sol–gel Sci. Tech.*, 1996, **6**, 7.
37 M. Shiozawa, K. Kitazumi, M. Iwai, S. Mizuno, N. Kato, Y. Takeda and T. Hamaguchi, *Electrocatalysis*, 2022, **13**, 830.
38 H. Effenberger, *Acta Crystallogr., Sect. C: Cryst. Struct. Commun.*, 1991, **47**, 2644.
39 N. E. Brese, M. O'Keeffe, B. L. Ramalkrishna and R. B. Von Dreele, *J. Solid State Chem.*, 1990, **89**, 184.
40 J. Lopitaux, J. C. Tellier, M. Lenglet and M. A. Erb, *Bull. Soc. Chim. Fr.*, 1973, 2909.
41 E. Prince and R. G. Treuting, *Acta Crystallogr.*, 1956, **9**, 1025.
42 A. Burg and D. Meyerstein, *Adv. Inorg. Chem.*, 2012, **64**, 219.
43 S. Park, J. H. Baek, L. Zhang, J. M. Lee, K. H. Stone, I. S. Cho, J. Guo, H. S. Jung and X. Zheng, *ACS Sustain. Chem. Eng.*, 2019, **7**, 5867.
44 N. J. Bernstein, S. A. Akhade and M. K. Janik, *Phys. Chem. Chem. Phys.*, 2014, **16**, 13708.
45 W. Luo, X. Nie, M. J. Janik and A. Asthagiri, *ACS Catal.*, 2016, **6**, 219.
46 J. H. Montoya, A. A. Peterson and J. K. Nørskov, *ChemCatChem*, 2013, **5**, 737.
47 S. Y. Choi, T. W. Kim, H. W. Jeong and H. Park, *Appl. Catal. A, General*, 2023, **654**, 119071.